Available online at www.sciencedirect.com
ScienceDirect
Infrared Physics & Technology 50 (2007) 279–283
INFRARED PHYSICS & TECHNOLOGY
www.elsevier.com/locate/infrared

Spin split-off transition based IR detectors operating at high temperatures

P.V.V. Jayaweera [a], S.G. Matsik [a], K. Tennakone [a], A.G.U. Perera [a,*], H.C. Liu [b], S. Krishna [c]

[a] *Department of Physics and Astronomy, Georgia State University, Atlanta, GA 30303, United States*
[b] *Institute for Microstructural Sciences, National Research Council, Ottawa, Canada K1A 0R6*
[c] *Center for High Technology Materials, University of New Mexico, Albuquerque, New Mexico 87101, USA*

Available online 9 November 2006

Abstract

GaAs/AlGaAs based Heterojunction Interfacial Workfunction Internal Photoemission (HEIWIP) detectors were used to demonstrate experimental split-off response that is based on hole transitions between light/heavy hole bands and the split-off band (spin-orbit). Preliminary results indicate that, this detection mechanism is more efficient than free carrier mechanism for NIR operation. An unoptimized, GaAs/AlGaAs detector with a free carrier threshold wavelength of $\sim$20 μm showed a maximum operating temperature of 130 K for split-off response in the range 1.5–5 μm with a peak D^* of 1.0×10^8 Jones. By adjusting the free carrier threshold to match the split-off threshold, it should be feasible to further increase the operating temperature. Analysis indicates that practical devices with properly optimized parameters are capable of achieving room temperature operation with higher specific detectivity. The possible ways to tailor the threshold, for the split-off response to different wavelength rangers using different materials such as phosphides and nitrites are also discussed.
© 2006 Elsevier B.V. All rights reserved.

PACS: 71.55.Eq; 71.70.−d; 71.70.Ej; 73.40.Ty

Keywords: Split-off; IR detector

The Infrared detection at room temperature is becoming important owing to the necessity of such detection techniques in a wide range of applications in the civilian, industrial, medical, astronomy and military sectors. Based on a well developed material system, GaAs/AlGaAs based Heterojunction Interfacial Workfunction Internal Photoemission (HEIWIP) detectors and Quantum Well Infrared (QWIP) detectors for MIR ($\lambda \sim$ 5–25 μm) to FIR ($\lambda >$ 25 μm) ranges have been demonstrated elsewhere [1–4]. One of the major constraints on the operating temperature of IR detectors is the need for a low dark current level to obtain reliable detection. In semiconductor devices, the dark current typically increases with temperature. Hence, the dark current limit effectively determines the operating temperature of a detector.

Split-off band effects have been observed in the emission of GaAs Metal Semiconductor Field Effect Transistors [5] and have enhanced the response of GaInAsP quantum wells [6]. This article describes NIR ($\lambda <$ 5 μm) response observed from the split-off (S-O) band of GaAs/AlGaAs HEIWIP detectors designed for the MIR and FIR ranges [7]. The active region of the basic HEIWIP detector consists of one or more periods, each consisting of a doped emitter and undoped barrier layers. In general, the detector can have several emitter/barrier periods, sandwiched between two highly doped contacts as shown in Fig. 1(a). Depending on the doping required for ohmic contacts, the top contact may also serve as the top emitter layer.

* Corresponding author. Tel.: +1 404 651 2709; fax: +1 404 651 1427.
E-mail addresses: viraj@phy-astr.gsu.edu (P.V.V. Jayaweera), uperera@gsu.edu (A.G.U. Perera).

1350-4495/$ - see front matter © 2006 Elsevier B.V. All rights reserved.
doi:10.1016/j.infrared.2006.10.007

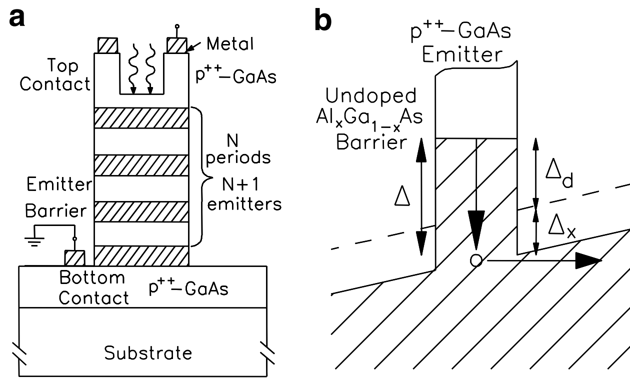

Fig. 1. (a) Typical structure of a GaAs emitter AlGaAs barrier HEIWIP detector. (b) Band diagram showing the workfunction (Δ) for photoemission of carriers. Here, Δ is given by $\Delta = \Delta_d + \Delta_x$ where Δ_d and Δ_x are the contributions from the doping and the Al fraction, respectively. The dashed lines indicate the valence-band edge if the barriers were GaAs.

A p-type band diagram for a single period of a detector is shown in Fig 1(b). Here, the workfunction (Δ) is given by $\Delta = \Delta_d + \Delta_x$ where Δ_d and Δ_x are the contributions from doping and the Al fraction, respectively. The dashed lines indicate the valence-band edge if the barriers were GaAs. As the Al fraction is reduced, Δ will be limited by Δ_d, which in turn is a homojunction detector.

The HEIWIP detectors designed for the MIR and FIR ranges showed NIR response peaks. These peaks appear on top of the free carrier response region, when the spectral sensitivity matches the GaAs S-O energy difference in the GaAs emitter based HEIWIPs. These relatively strong S-O responses can be seen up to 130 K, while the free carrier response disappeared beyond 40 K.

The S-O band IR detectors can be based on four detection mechanisms, with each depending on three processes; (i) the photoabsorption which generates the excited carriers, (ii) escape of the carriers, and (iii) the sweep out and collection of the escaped carriers. By having a high enough doping to have the scattering length similar to the emitter thickness, the carriers will scatter before the wave function can interfere with itself and hence will not form discreet quantum states inside the well. This makes the carrier distribution in the emitter three dimensional but still bound. For doping values used in these detectors the scattering length [8] is about 200 Å, close to thickness of the emitter. The absorption involves free carrier transitions, which is different from the response observed previously in Si/SiGe detectors [9] which used transitions from bound states to either a bound split-off band state, or a continuum state which is a mixture of the light, heavy and split-off hole bands. The Si/SiGe detectors are QWIPs operating in a bound-bound and bound-continuum mode. In explaining the detection mechanisms, three bands will have to be considered, the light hole (L-H) and heavy hole (H-H) bands which are degenerate at $k = 0$, and the S-O band which is separated from them by an energy E_{so}. Under equilibrium conditions, a p-doped region will have a Fermi level in the L-H and H-H bands, but above the S-O band maximum. The four detection mechanisms include the standard free carrier absorption described [10] before, and used in both homojunction [11,12] and heterojunction [13] detectors. The other three mechanisms can only occur for p-type detectors as they involve transitions between the hole bands. Once the carrier is in the S-O band, it can escape directly or scatter back into the L-H/H-H bands, and then escape.

(I) As seen in Fig. 2(a), for free carrier absorption in the emitter layers, the carriers remain in the L-H/H-H band. The excited carriers then escape from the emitter layer by internal photoemission at the interface between the emitters and barriers. The applied electric field will sweep the carriers out of the active region. This standard mechanism can also occur for electrons in the conduction band of n-type detectors.

(II) If the transition between the L-H/H-H band and the S-O band is direct, as shown in Fig. 2(b), the final energy of the excited carrier will not allow it to escape from the emitter while remaining in the S-O band. This is due to the energy of states in the S-O band with $k < k_f$ where k_f corresponds to the Fermi level in the heavy hole band being above the barrier in the S-O band. While it is possible to design a device in which the S-O states are below the barrier, such a device will have a low barrier height in the L-H/H-H bands, resulting in very high dark current. The carrier will scatter out of the S-O band back to the L-H/H-H band with an excited energy, and then will be able to escape by a process via the standard mechanism. Because of the occupation in the L-H/H-H bands, this scattering time should be faster than a direct relaxation.

(III) For an indirect transition, it is possible for the excited carrier to have $k > k_f$ which means the carrier can have sufficient energy to escape directly in the S-O band Fig. 2(c). In this case the escape process will be similar to that of the standard mechanism, with carriers in the escape cone passing over the barrier, and the remainder of the carriers trapping in the emitter region.

(IV) For indirect transitions in which the carriers do not end up in the escape cone Fig. 2(d), it is still possible to go through the scattering process as in mechanism II in order to escape. Here process A is an indirect photoabsorption, followed by a scattering event to the L-H or H-H band. The internal photoemission then occurs in the L-H or H-H band. This process provides an additional escape route for carriers in mechanism III that are not in the escape cone, as well as allowing carriers resulting from absorption of lower energy photons that would not have any possibility of escape in the S-O band. The threshold here is determined by the difference between the Fermi energy and the S-O band edge.

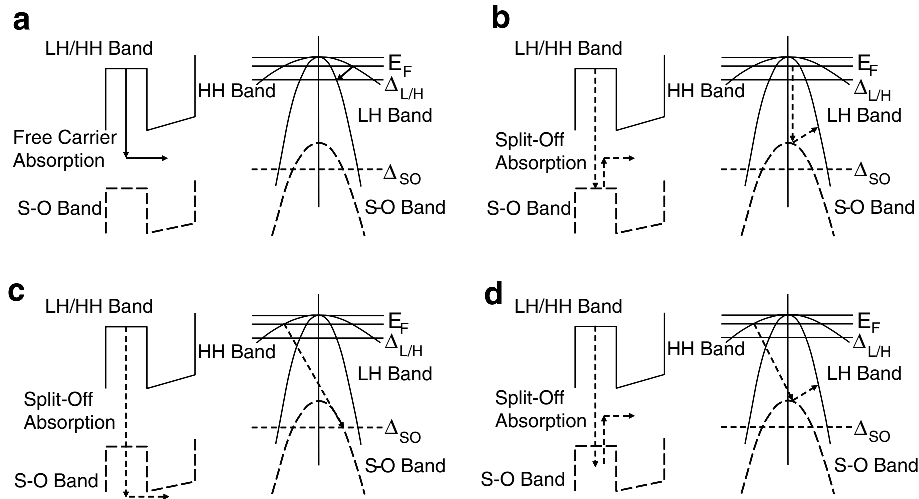

Fig. 2. Band diagram of the hole bands (light hole – LH and heavy hole – HH) and an energy diagram illustrating (a) the standard HEIWIP response mechanism and (b–d) the Split-off (S-O) band mechanisms. The S-O response can be categorized as (b) direct absorption, (c) indirect absorption without scattering, (d) indirect absorption with scattering. Actions involving the S-O band as either the initial or final state are indicated by dashed arrows. The horizontal lines indicate the barrier ($\Delta_{L/H}$ and Δ_{SO} for the LH/HH and S-O holes, respectively) and Fermi (E_F) energies.

Two groups of detectors were used in this study. The S-O response is first shown using a detector designed for the 10–15 μm range with a 20 μm threshold [2], which was not designed for optimum S-O response. The detector HE0204 design consisted of 16 periods of p-doped 188 Å GaAs emitters doped to 10^{18} cm^{-3} with carbon and 1250 Å $Al_{0.12}Ga_{0.88}As$ barriers. The top and bottom contacts were 1×10^{19} cm^{-3} p-doped GaAs layers with 0.2 and 0.7 μm thicknesses respectively. The detectors were made by wet etching to form square mesas with sides 400, 600, 800, and 1000 μm. Ti/Pt/Au ohmic contacts were evaporated onto the top and bottom contact layers. A ring contact is used on the top surface and square windows of 260, 460, 660, or 860 μm sides are open to allow front illumination. The top contact was thinned to roughly 1000 Å (with ∼100 Å depleted) leaving 900 Å of the top contact to serve as the first emitter layer giving a total of 17 emitters. The processed detector is shown in Fig. 1(a).

Dark current variation with bias voltage for HE0204 at various temperatures is shown in Fig. 3. The measured responsivity in the 1.5–5 μm S-O range for HE0204 at 79–130 K is shown in Fig. 4. A peak response of 0.45 A/W was seen at 105 K at 2.0 μm. The response increased when the temperature was increased from 79 K giving the highest response at 105 K. As the temperature was further increased, the response decreased, and was not measured beyond 130 K. The increase in response with temperature may be related to phonon effects on the escape rate for excited carriers. Further studies to investigate the temperature dependence are planned. The total quantum efficiency determined by dividing the photocurrent by the incident photon rate was ∼27%, and at 1.8 μm a specific detectivity (D^*) of 2.2×10^7 Jones was obtain at 90 K. This value is low due to the design of these detectors for operation at much lower temperatures. The increased barrier in

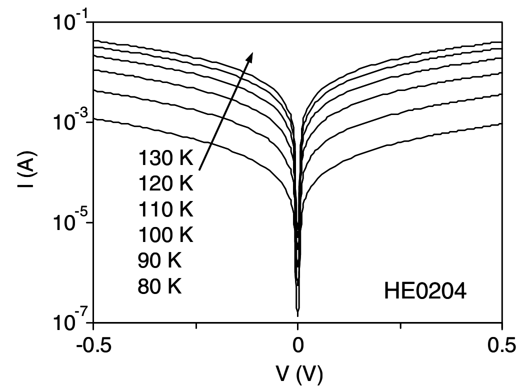

Fig. 3. Dark current variation with bias voltage for HE0204 at various temperatures.

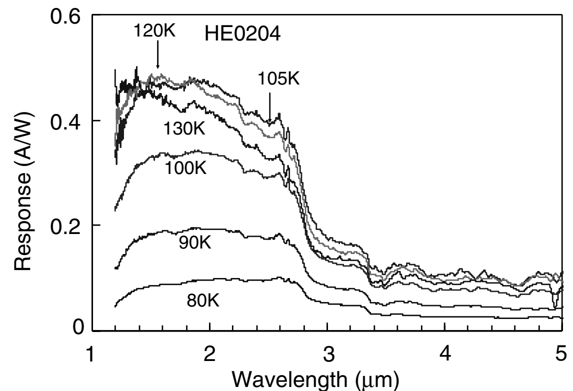

Fig. 4. Measured responsivity of detector HE0204 at various temperatures at 5 kV/cm bias field. The peak response was 0.45 mA/W at ∼2.0 μm. The response increased with temperature up to 105 K, and then decreased rapidly. The two steps indicated by arrows in the response at 2.8 μm and 3.4 μm are due to the thresholds for mechanisms III and II/IV, respectively.

an optimized detector should reduce the dark current and hence improve D^*. The two steps seen in the response at 2.8 and 3.4 μm are probably caused by the thresholds for mechanisms III, and II/IV, respectively. This indicates that the use of high doping is the preferred approach. A small signature could be identified at 3.7 μm which could possibly be a signature of the bound heavy-light hole to bound S-O transitions.

Based on previous experimental results and the standard thermionic current calculations, the dark current should not increase significantly, as doping is increased until the defect assisted tunneling dominates. If the doping is kept below these high values, the absorption is increased, therefore the response and hence the Background limited infrared photodetection temperature should increase.

The detector 1332 had 16 periods with 3.6×10^{18} cm^{-3} and 1.2×10^{18} cm^{-3} Be-doped top contact and emitters, respectively. The quantum efficiency of detector 1332 at 50 K and a bias field of 3 kV/cm is shown in Fig. 5. The broad response from 5 to 15 μm is due to the free carrier absorption and the sharp peak at 2–4 μm is due to the S-O response. This increased quantum efficiency is due to the increased absorption/emission in the S-O region. For free carrier and indirect absorption response (I, III, and IV), a phonon or an impurity scattering event is required in the absorption to conserve momentum, while in mechanisms II and IV, a scattering event is also required. Since mechanism IV requires two extra particles, it should be slower than the other three. The threshold for mechanism III will be shorter than for mechanisms II and IV due to the requirement of passing the barrier in the S-O band. Based on the width and two thresholds in the S-O response, both the direct and indirect absorptions are occurring in the S-O response.

In order to understand the strong response observed using the S-O band, calculations were carried out to determine the relative absorptions for the free carrier and S-O responses. The first step was to use a $k \cdot p$ model, similar to that used in quantum dots [14] and quantum wells to calculate the L-H, H-H and S-O hole energy bands. The absorption coefficient was then calculated as a function of photon energy $\hbar\omega$ from the energy states in the band. The calculation was done for a 1 μm thick GaAs layer p-doped to 1×10^{18} cm^{-3}. The absorption by the S-O band was over an order of magnitude larger than for the free carrier absorption in the L-H/H-H bands as shown in Fig. 6, indicating the relative improvement of the S-O mechanism in this range. As shown in Fig. 7 the measured absorption is increased in the split-off region compared to the expected free carrier absorption. The experimental quantum efficiency is larger than the calculated quantum efficiency (even with the increased experimental absorption taken into account). This difference is believed to be due to the gain resulting from the large split-off energy (~340 meV) for GaAs. The high energy for carriers that have been excited into the split-off band means that they will have sufficient energy to excite additional carriers via impact effects, intro-

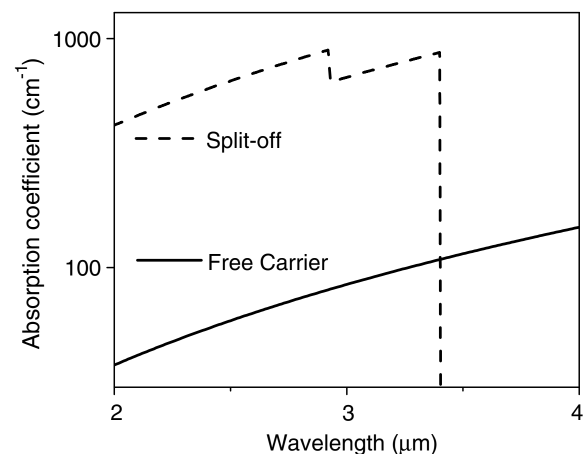

Fig. 6. The calculated absorption coefficient for the free carrier and the S-O band absorptions in a 3×10^{18} cm^{-3} p-doped GaAs layer. The steps in the S-O results correspond to the thresholds for mechanism III and II and/or IV. It is seen that the S-O absorption is much stronger than the free carrier absorption at shorter wavelengths.

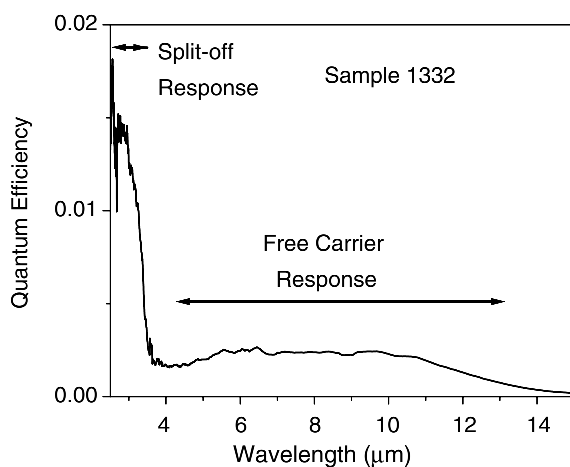

Fig. 5. The quantum efficiency of detector 1332 at 50 K and a bias field of 3 kV/cm.

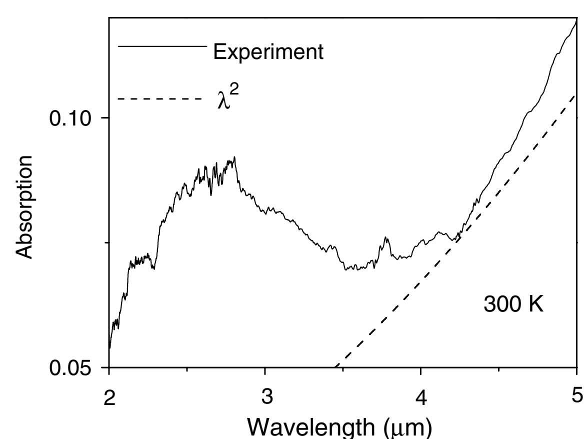

Fig. 7. Measured absorption for the sample HE0204 showing the increased absorption from the split-off response. The dashed line shows a λ^2 curve as is expected for the free carrier part of the response.

Table 1
The S-O band offset energy for different materials

Material	Δ_{SO} (meV)	λ_{SO} (μm)
InN	3	410
GaN	20	62
AlN	19	65
InP	108	11
GaP	80	16
AlP	70	18
InAs	390	3.2
GaAs	340	3.6
AlAs	280	4.4

Nitride and phosphide compounds are interest for wavelengths beyond 10 μm.

ducing a high gain factor into the detectors. The step seen in response at 3.4 μm is in good agreement with the calculated results shown in Fig. 6. However, there is a small discrepancy with the drop calculated to occur at 2.9 μm. The experimental step is ~0.15 μm wide, (possibly due to the effects of the photoemission process) and the threshold may be longer than it appears in Fig. 4. The difference in the response between the mechanisms is larger than is seen in the absorption coefficient calculation. This is probably due to differences in the escape probability for the different mechanisms. Future work is planned to calculate the escape probabilities of the mechanisms, obtaining a complete response model for the S-O band detectors.

The tested devices with a threshold of ~20 μm showed a maximum operating temperature of 130 K. By reducing the threshold to ~5 μm, the operating temperature should be increased to 300 K with D^* of $\sim 5 \times 10^9$ Jones. The response can be optimized by increasing number of layers in order to improve absorption, using surface plasmon resonances in metallic nanoparticles deposited on the detector surface [15]. Properly optimized device working at room temperature may compete with currently available uncooled detectors [16,17]. Materials other than GaAs/AlGaAs may lead to improved coverage in the 3–5 μm range. A direct transition to the S-O band for InP gives a threshold of 11 μm, while the nitride materials may be able to operate at 60 μm or beyond in the S-O mode as seen from Table 1. By using different materials as shown in Table 1, it should be possible to tailor the threshold for the S-O response to different wavelength ranges. The research will look at which materials are optimal for use in the different spectral ranges, with the emphasis on the 10–15 μm range for which the phosphides should be the best.

Acknowledgements

This work is supported by the NSF under Grant No. ECS 05-53051 and INT-0322355.

References

[1] M. Jhabvala, K. Choi, A.C. Goldberg, A.T. La, S.D. Gunapala, Development of a 1K × 1K GaAs QWIP far IR imaging array, presented at Focal Plane Arrays for Space Telescopes, SPIE 5167 (2004) 175.

[2] S.G. Matsik, M.B.M. Rinzan, D.G. Esaev, A.G.U. Perera, H.C. Liu, M. Buchanan, 20 μm cutoff heterojunction interfacial work function internal photoemission detectors, Appl. Phys. Lett. 84 (2004) 3435–3437.

[3] M.B.M. Rinzan, A.G.U. Perera, S.G. Matsik, H.C. Liu, Z.R. Wasilewski, M. Buchanan, AlGaAs emitter/GaAs barrier terahertz detector with a 2.3 THz threshold, Appl. Phys. Lett. 86 (2005) 071112.

[4] A.G.U. Perera, W.Z. Shen, S.G. Matsik, H.C. Liu, M. Buchanan, W.J. Schaff, GaAs/AlGaAs quantum well photodetectors with a cutoff wavelength at 28 μm, Appl. Phys. Lett. 72 (1998) 1596–1598.

[5] K.S. Zhuravlev, V.A. Kolosanov, A.G. Milekhin, V.G. Polovinkin, T.S. Shamirzaev, Yu N. Rakov, Yu B. Myakishev, J. Fryar, E. McGlynn, M.O. Henry, Infrared light emission from GaAs MESFETs operating at avalanche breakdown conditions, Semicond. Sci. Technol. 19 (2004) S94–S95.

[6] J.R. Hoff, M. Razeghi, G.J. Brown, Effect of the spin split-off band on optical absorption in p-type $Ga_{1-x}In_xAs_yP_{1-y}$ quantum-well infrared detectors, Phys. Rev. B 54 (1996) 10773–10783.

[7] D.G. Esaev, M.B.M. Rinzan, S.G. Matsik, A.G.U. Perera, Design and optimization of GaAs/AlGaAs heterojunction infrared detectors, J. Appl. Phys. 96 (2004) 4588–4597.

[8] J. Maserjian, Long-wave infrared (LWIR) detectors based on III–V materials, SPIE 1540 (1991) 127.

[9] R.P.G. Karunasiri, J.S. Park, K.L. Wang, Normal incidence infrared detector using intervalence-subband transitions in $Si_{1-x}Ge_x$/Si quantum wells, Appl. Phys. Lett. 62 (1992) 2434.

[10] A.G.U. Perera, H.X. Yuan, M.H. Francombe, Homojunction internal photoemission far-infrared detectors: photoresponse performance analysis, J. Appl. Phys. 77 (1995) 915–924.

[11] A.G.U. Perera, H.X. Yuan, S.K. Gamage, W.Z. Shen, M.H. Francombe, H.C. Liu, M. Buchanan, W.J. Schaff, GaAs multilayer p^+-i homojunction far-infrared detectors, J. Appl. Phys. 81 (1997) 3316.

[12] A.G.U. Perera, W.Z. Shen, H.C. Liu, M. Buchanan, M.O. Tanner, K.L. Wang, Demonstration of Si homojunction far-infrared detectors, Appl. Phys. Lett. 72 (1998) 2307.

[13] A.G.U. Perera, S.G. Matsik, B. Yaldiz, H.C. Liu, A. Shen, M. Gao, Z.R. Wasilewski, M. Buchanan, Heterojunction wavelength-tailorable far-infrared photodetectors with response out to 70 μm, Appl. Phys. Lett. 78 (2001) 2241–2243.

[14] H. Jiang, J. Singh, Strain distribution and electronic spectra of InAs/GaAs self-assembled dots: An eight-band study, Phys. Rev. B 56 (1997) 4696–4701.

[15] D.M. Schaadt, B. Feng, E.T. Yu, Enhanced semiconductor optical absorption via surface plasmon excitation in metal nanoparticles, Appl. Phys. Lett. 86 (2005) 063106-3.

[16] A. Rogalski, Optical detectors for focal plane arrays, Opto-Electron. Rev. 12 (2004) 221–245.

[17] M.Z. Tidrow, W.W. Clark Iii, W. Tipton, R. Hoffman, W.A. Beck, S.C. Tidrow, D.N. Robertson, H.K. Pollehn, K.R. Udayakumar, H.R. Beratan, K.L. Soch, C.M. Hanson, M. Wigdor, Uncooled infrared detectors and focal plane arrays, presented at Detectors, Focal Plane Arrays, and Imaging Devices II, Beijing, China, 1998.